

Near-field ultrafast nanoscopy of carrier dynamics in silicon nanowires

Jingang Li^{1,7}, Rundi Yang^{1,7}, Yoonsoo Rho^{1,2}, Penghong Ci^{3,4,5}, Matthew Eliceiri¹, Hee K. Park⁶, Junqiao Wu^{3,4}, and Costas P. Grigoropoulos^{1*}*

¹ Laser Thermal Laboratory, Department of Mechanical Engineering, University of California, Berkeley, California 94720, USA

² Physical and Life Sciences and NIF and Photon Sciences, Lawrence Livermore National Laboratory, Livermore CA 94550, USA

³ Department of Materials Science and Engineering, University of California, Berkeley, California 94720, USA

⁴ Materials Sciences Division, Lawrence Berkeley National Laboratory, Berkeley, California 94720, USA

⁵ Institute for Advanced Study, Shenzhen University, Shenzhen 518060, China

⁶*Laser Prismatic, LLC, San Jose, USA*

⁷ These authors contributed equally to this work.

*Email: cgrigoro@berkeley.edu (C.P.G.), hirho@berkeley.edu (Y.R.)

Abstract

Carrier distribution and dynamics in semiconductor materials often govern their physics properties that are critical to functionalities and performance in industry applications. The continued miniaturization of electronic and photonic devices calls for new tools to probe carrier behavior in semiconductors simultaneously at the picosecond time scale and nanometer length scale. Here, we develop pump-probe scattering-type scanning near-field optical microscopy (s-SNOM) to characterize the carrier dynamics in semiconductor nanowires. By coupling experiments with the point-dipole model, we resolve the size-dependent photoexcited carrier lifetime in individual silicon nanowires. We further demonstrate local carrier decay time mapping in silicon nanostructures with a sub-50 nm spatial resolution. Our pump-probe s-SNOM enables the nanoimaging of ultrafast carrier kinetics, which is an important step to advance the future design of a broad range of electronic, photonic, and optoelectronic devices.

Introduction

Semiconductor technology has stimulated the exponential progress of microelectronics in the last half-century. Silicon-based complementary metal-oxide-semiconductor (CMOS) integrated circuits form the backbone of modern technology¹. In addition to the prevalence in electronic devices, silicon nanostructures are widely exploited in photonics for versatile control of light propagation, detection, and modulation²⁻⁵. Recently, the emerging low-dimensional quantum materials, particularly silicon nanowires (SiNWs), have also opened new possibilities for broad applications in electronics, photonics, photovoltaics, and photoelectrochemistry⁶⁻⁹.

For most semiconductor materials, free-carrier concentration determines their electrical and optical properties, such as conductivity, refractive index, and absorption coefficients¹⁰⁻¹². In addition, the performance of transistors and semiconductor devices primarily depends on the spatial and temporal carrier distribution¹³⁻¹⁵. Therefore, resolving the charge transport and carrier dynamics in semiconductor nanostructures is essential for designing future electronic and photonic devices.

Time-resolved terahertz spectroscopy has been widely applied to reveal carrier dynamics in bulk and nanostructured semiconductors^{16,17}. In addition, pump-probe microscopy was developed to probe the site-specific carrier transport and recombination¹⁸⁻²⁰. However, the spatial resolution of this microscopic method is limited by optical diffraction. Alternatively, tip-based scattering-type scanning near-field optical microscopy (s-SNOM) is capable of mapping free-carrier distribution in semiconductor nanostructures with a nanoscale resolution^{21,22}.

Here, we report the spatiotemporal nanoimaging of the carrier dynamics in semiconductor nanowires using pump-probe s-SNOM. We unravel the photoexcited carrier recombination dynamics by combining ultrafast near-field measurements and theoretical modeling. Moreover, this method enables the spatial mapping of carrier lifetime with a sub-50 nm resolution. Our results provide a new route to probe carrier behaviors in nanoscale materials and devices, which is of great significance to understanding the optoelectronic properties and practical functionality of semiconductor nanostructures.

Results

Fig. 1a shows the schematic of our pump-probe s-SNOM setup. A 400 nm pump beam and an 800 nm probe beam with a controlled delay time Δt are directed to an atomic force microscope (AFM) tip with an oscillating frequency Ω (see Methods and Supplementary Fig. 1 for more details on the setup). The backscattered probe beam is detected and demodulated at higher harmonics of the tapping frequency ($n\Omega$) to suppress background noise and amplify the near-field signal²³. The samples in this study are SiNWs synthesized via an electroless etching method (Inset in Fig. 1i)²⁴. Fig. 1b and Figs.1c-g show the topography of a SiNW and the time-resolved s-SNOM imaging at different time delays, respectively. The high spatial overlap of the height and s-SNOM profiles indicates the successful detection of near-field signals (Fig. 1h). The s-SNOM time snapshots distinctly exhibit a dynamic change in the intensity of scattered light (Fig. 1j). Specifically, the s-SNOM signal amplitude undergoes an intense increase (Fig.

1d), followed by a decay process (Figs. 1e,f) and a slow rise at longer delay times (Fig. 1g). This trend can also be quantitatively visualized in the transient s-SNOM signal presented in Fig. 1i.

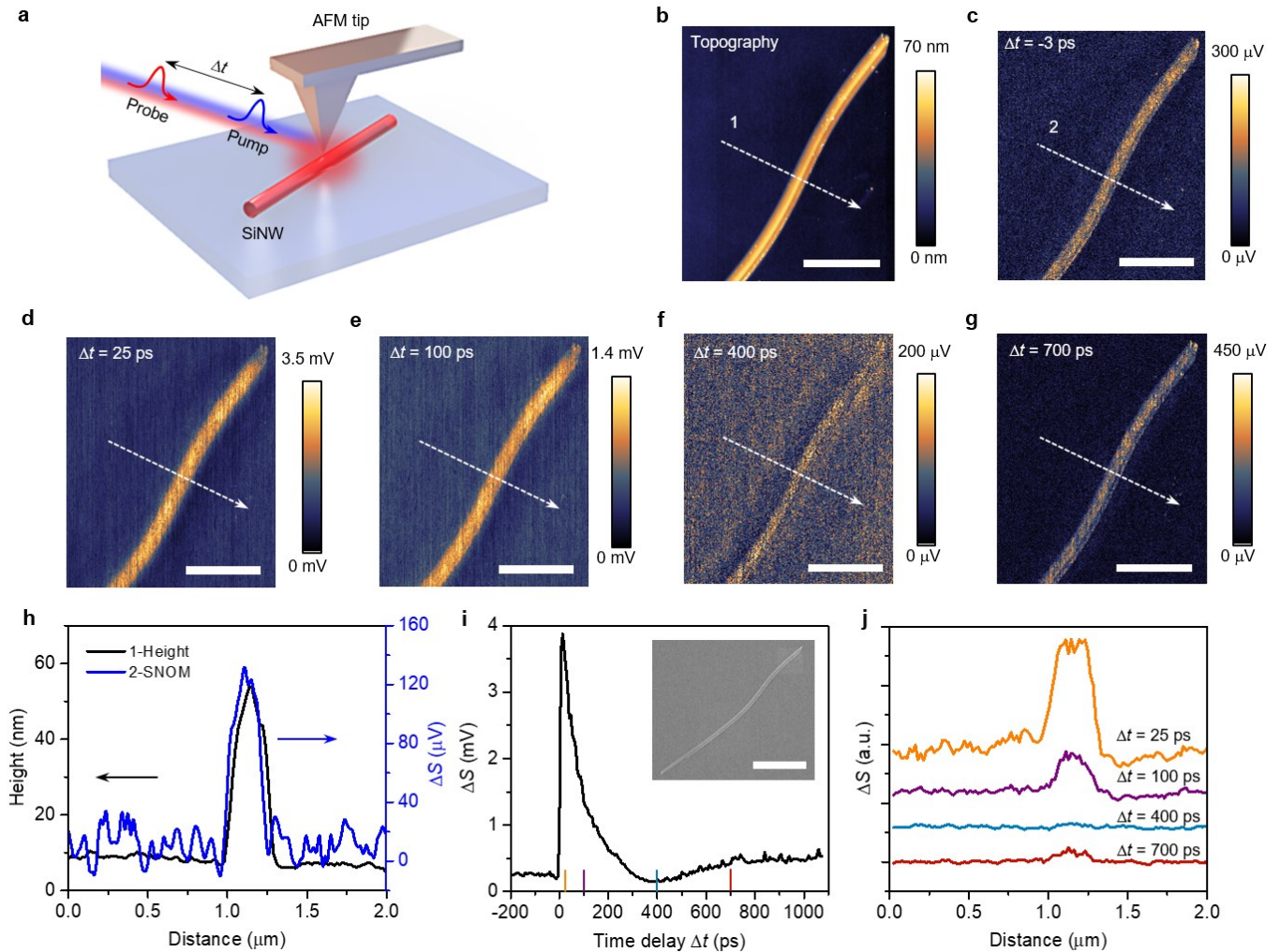


Fig. 1. Time-resolved s-SNOM imaging of a SiNW. **a**, Schematic of the pump-probe s-SNOM setup. The wavelengths of pump and probe beams are 400 and 800 nm, respectively. **B**, AFM topography of a SiNW. **c-g**, Time-resolved s-SNOM imaging of the SiNW with a pump-probe delay time of (c) -3 ps, (d) 25 ps, (e) 100 ps, (f) 400 ps, and (g) 700 ps. **h**, Height and s-SNOM profiles along the dashed lines in (b) and (c). **i**, Transient s-SNOM signal as a function of delay time. Inset shows the SEM image of the SiNW. **j**, s-SNOM line profiles across the SiNW at different pump-probe delay times in (d-g). Scale bars: (b-g) 1 μm , Inset in (i): 2 μm .

To understand the evolution of the s-SNOM signal over the increasing delay time, we adopt a point-dipole model to analyze the scattered light (see Supplementary Note 1)^{22,25,26}. Briefly, the scattered field \mathbf{E}_{sc} by the tip is derived from the dipolar near-field interaction between the AFM tip and the sample with the dielectric function ε , yielding^{25,26}

$$\mathbf{E}_{\text{sc}} \propto A e^{i\varphi} \mathbf{E}_{\text{in}} = \frac{\alpha(1+\beta)}{1 - \frac{\alpha\beta}{16\pi(a+z)^3}} \mathbf{E}_{\text{in}} \quad (1)$$

Here the measured scattering intensity $S \propto A^2$, φ is the phase of scattered light, a is the AFM tip radius, z is the tip-sample distance, $\alpha = 4\pi a^3$ is the polarizability of the tip, and $\beta = (\varepsilon - 1)/(\varepsilon + 1)$, respectively (Fig. 2a). The dielectric function ε is further calculated as a function of free carrier density N based on the Drude model (Supplementary Fig. 2)²⁷

$$\varepsilon(\omega) = \varepsilon_{\infty} - \frac{\omega_p^2}{\omega(\omega + i\Gamma)} \quad (2)$$

where $\varepsilon_{\infty} = 11.7$ for silicon, ω_p is the plasma frequency and a function of the carrier concentration N (Supplementary Note 2), and Γ is the damping rate. In addition, the effect of temperature is considered by the Jellison-Modine model²⁸ (Supplementary Fig. 3, also see Supplementary Note 2 for more details).

Fig. 2b shows the calculated s-SNOM intensity with an increasing free-carrier concentration N from 10^{18} to 10^{22} cm^{-3} at the wavelength of 800 nm. As N increases, the calculated s-SNOM signal exhibits a minimum at $N \sim 6 \times 10^{19}$ cm^{-3} and then reaches its maximum at $N \sim 1.2 \times 10^{20}$ cm^{-3} . This behavior arises from the resonant near-field interaction between the AFM probing tip and the free carriers in SiNWs²⁵. The experimental transient s-SNOM signal can be well fitted by the point-dipole model assuming a biexponential decay of photoexcited carriers, i.e., $N(\Delta t) = N(0) \times (A_1 e^{-\frac{\Delta t}{t_1}} + A_2 e^{-\frac{\Delta t}{t_2}})$ (Fig. 2c). This biexponential kinetics (t_1 , t_2) is attributed to the carrier recombination and diffusion²⁹, and the average carrier lifetime t_{avg} can be calculated by $t_{\text{avg}} = (A_1 + A_2)/(A_1/t_1 + A_2/t_2)$. The corresponding phase change is also consistent with the experimental results (Supplementary Fig. 4). We exclude the effect of laser heating as the temperature increase is negligible with respect to the s-SNOM amplitude

(Supplementary Note 3 and Supplementary Fig. 5). In addition, the variation of tip-sample distance due to thermal expansion of SiNWs only leads to slight changes in the s-SNOM intensity (Supplementary Note 4 and Supplementary Fig. 6). These results verify the dominant role of carrier density in the transient s-SNOM measurement. We further validate the point-dipole model by measuring the same SiNW with different pump power (Fig. 2d), where two curves can be well fitted with different initial carrier densities and the same decay kinetics (Supplementary Table 1).

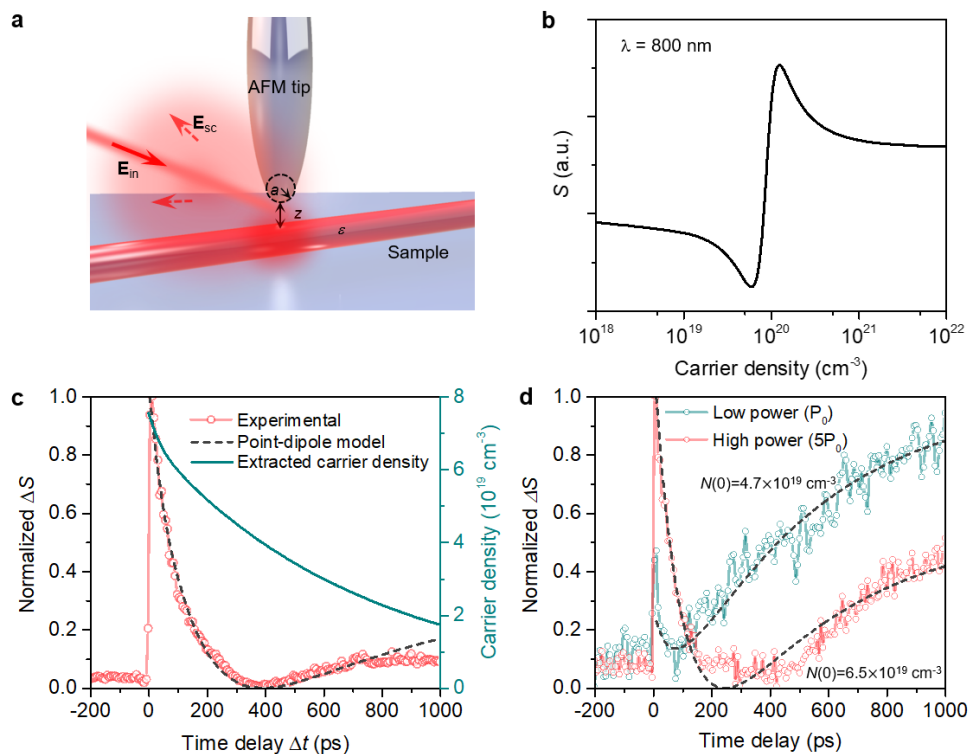


Fig. 2. Point-dipole modeling. **a**, Schematic of the point-dipole model. a , z , and ϵ are the AFM tip radius, tip-sample distance, and the permittivity of the sample, respectively. **b**, Modeled s-SNOM intensity as a function of carrier density in SiNWs. **c**, Experimental transient s-SNOM signal, fitting curve with the point-dipole model, and the extracted carrier density in SiNW as a function of pump-probe delay time. **d**, Experimental transient s-SNOM scans and fitting curves under different pump excitation powers.

We then apply pump-probe s-SNOM to investigate the carrier dynamics in individual SiNWs with varying geometries. Fig. 3a shows the transient s-SNOM signals measured at different nanowires with

various widths. The corresponding scanning electron microscope (SEM) images are shown in Fig. 3b. All experimental curves are well fitted with the point-dipole model, and the decay times are summarized in Fig. 3c. The carrier lifetime shows a linear increase with the increasing size of SiNW, which agrees with the predominant surface recombination in semiconductor nanowires³⁰. The surface recombination velocity (SRV) can be calculated from carrier lifetime t_{avg} as $\text{SRV} = d/4t_{\text{avg}}$, where d is the SiNW width³¹. The linear fitting gives a surface recombination velocity of 2.2×10^4 cm/s, which is consistent with previous reports^{29,32}.

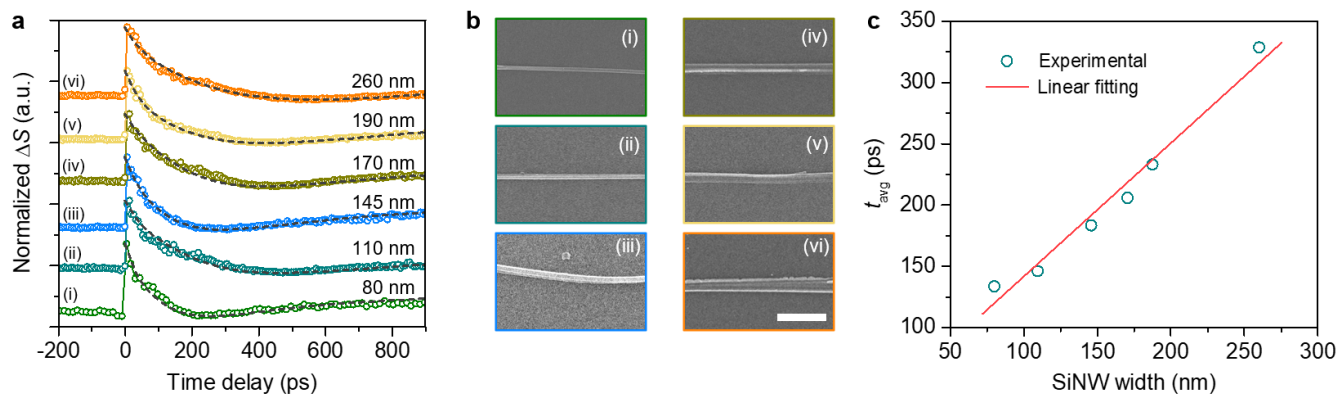


Fig. 3. Size-dependent carrier dynamics. **a**, Experimental transient s-SNOM scans measured from SiNWs with different widths (i) to (vi). The grey dashed curves present the fitting results by the point-dipole model. **b**, Corresponding SEM images of the SiNWs in (a). **c**, Size-dependent average decay time and the linear fitting. Scale bar: 1 μm .

We further explore the capability of pump-probe s-SNOM to probe the spatially resolved carrier dynamics with a nanoscale resolution. A large, nonuniform silicon nanowire is selected as the test sample (Fig. 4a). Transient s-SNOM signals measured at different locations (P1-P4 in Fig. 4a) show distinct evolution behaviors (Fig. 4b), corresponding to carrier lifetimes of 460.3, 379.9, 294.6, and 338.0 ps, respectively. The time-resolved s-SNOM images also exhibit spatially nonuniform dynamics of the nanostructure (Supplementary Fig. 7). Fig. 4c presents the time-resolved s-SNOM map along the nanowire (dashed line in Fig. 4a). The carrier lifetime extracted from the spatiotemporal mapping shows a similar

size-dependent trend, which matches well with the topographical profile (Fig. 4d). The probe of carrier dynamics at a spatial resolution of 35 nm is demonstrated.

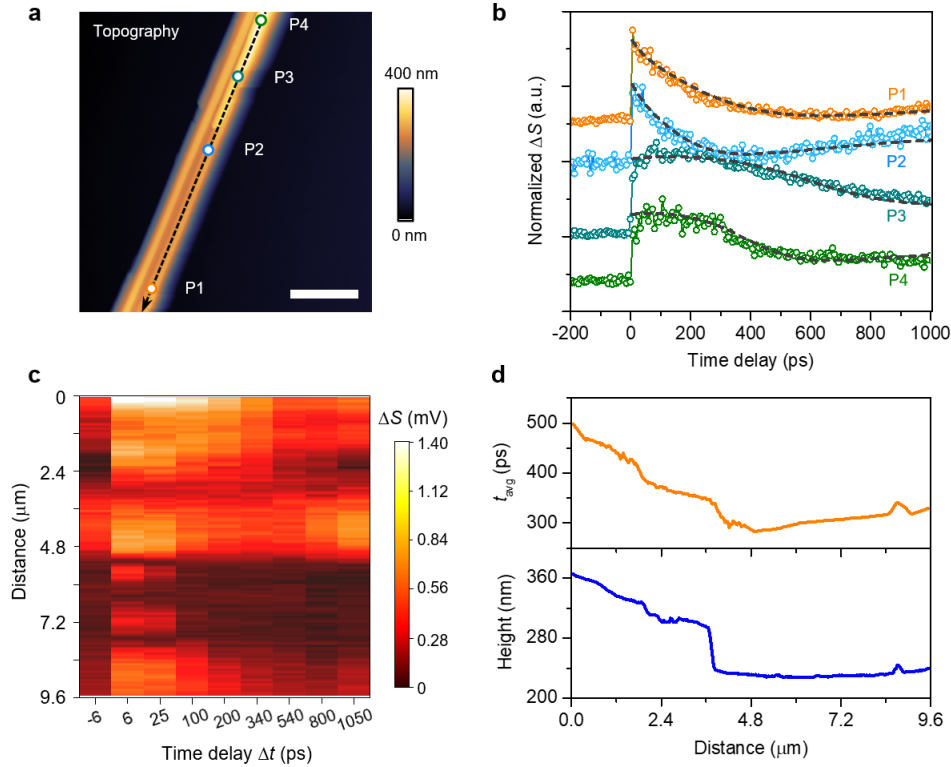


Fig. 4. Probing spatially resolved carrier dynamics at the nanoscale. **a**, AFM topography of a nonuniform silicon nanowire structure. **b**, Experimental transient s-SNOM scans and fitting curves measured at different locations, as marked in **(a)**. **c**, Time-resolved s-SNOM mapping along the dashed line in **(a)**. **d**, Corresponding decay time and height profiles with a spatial resolution of 35 nm. Scale bar: 2 μm .

Discussion

We have developed a pump-probe s-SNOM as a noninvasive technique to examine the carrier dynamics in semiconductor nanostructures. The combination of ultrafast optics and near-field imaging enables the investigation of carrier kinetics with both high temporal (picosecond) and spatial (sub-50 nm) resolutions. This capability is valuable for the characterization and optimization of functional optoelectronic devices. While this work analyzed the carrier dynamics in SiNWs as a demonstration, the pump-probe s-SNOM can serve as a versatile and general optical diagnostic platform to study nanomaterials, including two-

dimensional heterostructures³³ and quantum dots³⁴. It also provides a promising tool to study other non-equilibrium thermodynamic phenomena, including phase transitions^{35,36}, energy and charge transfer³⁷, and phonon propagation³⁸.

Methods

Experimental setup. The detailed schematic of the experimental setup is shown in Supplementary Fig. 1. The setup is developed based on a commercial near-field optical microscopy system from Molecular Vista. An 800 nm femtosecond laser beam (Spectra Physics) is split by a 9:1 beam splitter (CVI Laser Optics) into a probe beam (10%) and a pump beam (90%). The pump beam is frequency doubled by a nonlinear crystal, beta Barium borate (Eksma Optics), and then amplitude-modulated by an acoustic-optic modulator. The probe beam passes through a mechanical delay stage (Thorlabs). Both beams are merged and directed to the platinum-coated AFM tip (Molecular Vista) via a parabolic mirror. The optical intensities of pump and probe beams before entering the AFM chamber are ~ 1 mW and ~ 0.5 mW, respectively. The tip has a resonance frequency Ω at ~ 250 kHz and an apex radius of ~ 20 nm). The scattered probe light is then collected by the parabolic mirror and redirected to an avalanche photodiode detector (Thorlabs) after passing a long-pass filter (Thorlabs). The voltage signal from the avalanche photodiode detector (Thorlabs) is sent to a lock-in amplifier for signal demodulation, referenced at a frequency determined by the controller.

Characterizations. All SEM images are taken with a FEI Quanta 650 SEM.

Acknowledgments

We thank Zhengliang Su and Qiye Zheng for their assistance in the experimental setup. C.P.G. acknowledges the financial support from Laser Primitives under the DOE SBIR Phase 2 grant DE-SC0018461. This work is partly prepared by LLNL under Contract DE-AC52-07NA27344. The nanowire preparation was supported by the U.S. Department of Energy, Office of Science, Office of Basic Energy

Sciences, Materials Sciences and Engineering Division under Contract No. DE-AC02-05-CH11231 (EMAT program KC1201).

Author Contributions

J.L., Y.R., and C.P.G. conceived the idea and planned the experimental work. J.L., R.Y., and Y.R. worked on the experiments and analyzed the data. P.C. and J.W. synthesized the silicon nanowires. M.E. assisted in the experiments. H.K.P. contributed to the experimental design and apparatus construction. J.L. wrote the paper with inputs from all authors. C.P.G. supervised the project.

Competing interests

The authors declare no competing interests.

References

- 1 Zwanenburg, F. A. et al. Silicon quantum electronics. *Rev. Mod. Phys.* **85**, 961-1019 (2013).
- 2 Staude, I. & Schilling, J. Metamaterial-inspired silicon nanophotonics. *Nat. Photonics* **11**, 274 (2017).
- 3 Molesky, S. et al. Inverse design in nanophotonics. *Nat. Photonics* **12**, 659-670 (2018).
- 4 Leuthold, J., Koos, C. & Freude, W. Nonlinear silicon photonics. *Nat. Photonics* **4**, 535-544 (2010).
- 5 Li, J. et al. Tunable chiral optics in all-solid-phase reconfigurable dielectric nanostructures. *Nano Lett.* **21**, 973-979 (2021).
- 6 Deng, J. et al. Nanowire photoelectrochemistry. *Chem. Rev.* **119**, 9221-9259 (2019).
- 7 Jia, C., Lin, Z., Huang, Y. & Duan, X. Nanowire electronics: From nanoscale to macroscale. *Chem. Rev.* (2019).
- 8 Quan, L. N., Kang, J., Ning, C.-Z. & Yang, P. Nanowires for photonics. *Chem. Rev.* **119**, 9153-9169 (2019).
- 9 Garnett, E. C., Brongersma, M. L., Cui, Y. & McGehee, M. D. Nanowire solar cells. *Annu. Rev. Mater. Res.* **41**, 269-295 (2011).
- 10 Almeida, V. R., Barrios, C. A., Panepucci, R. R. & Lipson, M. All-optical control of light on a silicon chip. *Nature* **431**, 1081-1084 (2004).
- 11 Preble, S. F., Xu, Q. & Lipson, M. Changing the colour of light in a silicon resonator. *Nat. Photonics* **1**, 293-296 (2007).

- 12 Villora, E. G. et al. Electrical conductivity and carrier concentration control in β -ga₂o₃ by si doping. *Appl. Phys. Lett.* **92**, 202120 (2008).
- 13 Zaumseil, J., Friend, R. H. & Sirringhaus, H. Spatial control of the recombination zone in an ambipolar light-emitting organic transistor. *Nat. Mater.* **5**, 69-74 (2006).
- 14 Manaka, T., Lim, E., Tamura, R. & Iwamoto, M. Direct imaging of carrier motion in organic transistors by optical second-harmonic generation. *Nat. Photonics* **1**, 581-584 (2007).
- 15 Schlaepfer, F. et al. Attosecond optical-field-enhanced carrier injection into the gaas conduction band. *Nat. Phys.* **14**, 560-564 (2018).
- 16 Ulbricht, R. et al. Carrier dynamics in semiconductors studied with time-resolved terahertz spectroscopy. *Rev. Mod. Phys.* **83**, 543-586 (2011).
- 17 Parkinson, P. et al. Carrier lifetime and mobility enhancement in nearly defect-free core-shell nanowires measured using time-resolved terahertz spectroscopy. *Nano Lett.* **9**, 3349-3353 (2009).
- 18 Gabriel, M. M. et al. Imaging charge separation and carrier recombination in nanowire p-i-n junctions using ultrafast microscopy. *Nano Lett.* **14**, 3079-3087 (2014).
- 19 Grumstrup, E. M. et al. Reversible strain-induced electron-hole recombination in silicon nanowires observed with femtosecond pump-probe microscopy. *Nano Lett.* **14**, 6287-6292 (2014).
- 20 Cating, E. E. M. et al. Imaging spatial variations in the dissipation and transport of thermal energy within individual silicon nanowires using ultrafast microscopy. *Nano Lett.* **16**, 434-439 (2016).
- 21 Ritchie, E. T. et al. Mapping free-carriers in multijunction silicon nanowires using infrared near-field optical microscopy. *Nano Lett.* **17**, 6591-6597 (2017).
- 22 Stiegler, J. M. et al. Nanoscale free-carrier profiling of individual semiconductor nanowires by infrared near-field nanoscopy. *Nano Lett.* **10**, 1387-1392 (2010).
- 23 Chen, X. et al. Modern scattering-type scanning near-field optical microscopy for advanced material research. *Adv. Mater.* **31**, 1804774 (2019).
- 24 Ci, P. et al. Giant isotope effect of thermal conductivity in silicon nanowires. *Phys. Rev. Lett.* **128**, 085901 (2022).
- 25 Huber, A. J. et al. Simultaneous ir material recognition and conductivity mapping by nanoscale near-field microscopy. *Adv. Mater.* **19**, 2209-2212 (2007).
- 26 Knoll, B. & Keilmann, F. Infrared conductivity mapping for nanoelectronics. *Appl. Phys. Lett.* **77**, 3980-3982 (2000).
- 27 van Exter, M. & Grischkowsky, D. Carrier dynamics of electrons and holes in moderately doped silicon. *Phys. Rev. B* **41**, 12140-12149 (1990).
- 28 Jr., G. E. J. & Modine, F. A. Optical functions of silicon at elevated temperatures. *J. Appl. Phys.* **76**, 3758-3761 (1994).
- 29 Gabriel, M. M. et al. Direct imaging of free carrier and trap carrier motion in silicon nanowires by spatially-separated femtosecond pump-probe microscopy. *Nano Lett.* **13**, 1336-1340 (2013).

- 30 Dan, Y. et al. Dramatic reduction of surface recombination by in situ surface passivation of silicon nanowires. *Nano Lett.* **11**, 2527-2532 (2011).
- 31 Mohite, A. D. et al. Highly efficient charge separation and collection across in situ doped axial vls-grown si nanowire p–n junctions. *Nano Lett.* **12**, 1965-1971 (2012).
- 32 Christesen, J. D. et al. Design principles for photovoltaic devices based on si nanowires with axial or radial p–n junctions. *Nano Lett.* **12**, 6024-6029 (2012).
- 33 Zhang, Z. et al. Endoepitaxial growth of monolayer mosaic heterostructures. *Nat. Nanotechnol.* **17**, 493-499 (2022).
- 34 Zhang, Z. et al. Ultrafast exciton transport at early times in quantum dot solids. *Nat. Mater.* **21**, 533-539 (2022).
- 35 Dönges, S. A. et al. Ultrafast nanoimaging of the photoinduced phase transition dynamics in vo₂. *Nano Lett.* **16**, 3029-3035 (2016).
- 36 Sood, A. et al. Universal phase dynamics in vo₂ switches revealed by ultrafast operando diffraction. *Science* **373**, 352-355 (2021).
- 37 Tomko, J. A. et al. Long-lived modulation of plasmonic absorption by ballistic thermal injection. *Nat. Nanotechnol.* **16**, 47-51 (2021).
- 38 Qian, X., Zhou, J. & Chen, G. Phonon-engineered extreme thermal conductivity materials. *Nat. Mater.* **20**, 1188-1202 (2021).

Supplementary Notes

Supplementary Note 1. Point-dipole model

Point-dipole model provides a good qualitative description of the near-field interaction in scattering-type scanning near-field optical microscopy (s-SNOM)¹⁻³. The tip is reduced to a small sphere with a point dipole at its center. The scattered field is calculated based on the dipolar near-field coupling between the tip and sample. Briefly, the scattered field \mathbf{E}_{sc} can be written as

$$\mathbf{E}_{\text{sc}} \propto A e^{i\varphi} \mathbf{E}_{\text{in}} = \frac{\alpha(1+\beta)}{1 - \frac{\alpha\beta}{16\pi(a+z)^3}} \mathbf{E}_{\text{in}} \quad (\text{S1})$$

Here the measured scattering intensity $S \propto A^2$, φ is the phase of scattered light, a is the AFM tip radius, z is the tip-sample distance, $\alpha = 4\pi a^3$ is the polarizability of the tip, and $\beta = (\varepsilon - 1)/(\varepsilon + 1)$, respectively. In our case, $a = 20$ nm is used. ε is calculated based on the Drude model and the Jellison-Modine model to account for the effect of carrier density and temperature, respectively, which will be discussed in Supplementary Note 2. The time-resolved s-SNOM amplitude is calculated based on the biexponential decay of photocarriers

$$N(\Delta t) = N(0) \times (A_1 e^{-\frac{\Delta t}{t_1}} + A_2 e^{-\frac{\Delta t}{t_2}}) \quad (\text{S2})$$

where $N(0)$ is the initial carrier density right after the pump excitation, Δt is the pump-probe time delay, A_1 , A_2 , t_1 , and t_2 are fitting parameters with $A_1 + A_2 = 1$. The fitting of experimental curved is conducted in MATLAB based on a nonlinear least-squares algorithm to obtain the decay time parameters.

Supplementary Note 2. Modeling of the dielectric function ε

The dielectric function ε is modeled as a function of carrier density N by the Drude model⁴

$$\varepsilon(\omega) = \varepsilon_{\infty} - \frac{\omega_p^2}{\omega(\omega + i\Gamma)} \quad (\text{S3})$$

here $\varepsilon_{\infty} = 11.7$ for silicon, Γ is the damping rate, $\omega_p = \frac{Ne^2}{\varepsilon_0 m}$ is the plasma frequency where e is the elementary charge, ε_0 is the free-space permittivity, and m is the effective carrier mass. Γ is calculated by

$\Gamma = \frac{e}{m\mu}$, where μ is the carrier mobility. μ is determined as a function of N based on the empirical equations proposed by Arora and coworkers⁵.

In addition, the effect of temperature is considered by the Jellison-Modine model as⁶

$$n(\omega, T) = n_0(\omega) + a(\omega)T \quad (\text{S4})$$

$$k(\omega, T) = k_0(\omega)\exp\left(\frac{T}{T_0(\omega)}\right) \quad (\text{S5})$$

where $\omega_g = 3.648$ eV, $n_0(\omega) = \sqrt{4.565 + 97.3/(\omega_g^2 - \omega^2)}$, $a(\omega) = [-1.864 + 53.94/(\omega_g^2 - \omega^2)] \times 10^{-4}$, $k_0(\omega) = -0.0805 + \exp[-3.1893 + 7.946/(\omega_g^2 - \omega^2)]$, and $T_0(\omega) = 369.9 - \exp[-12.92 + 5.509\omega]$.

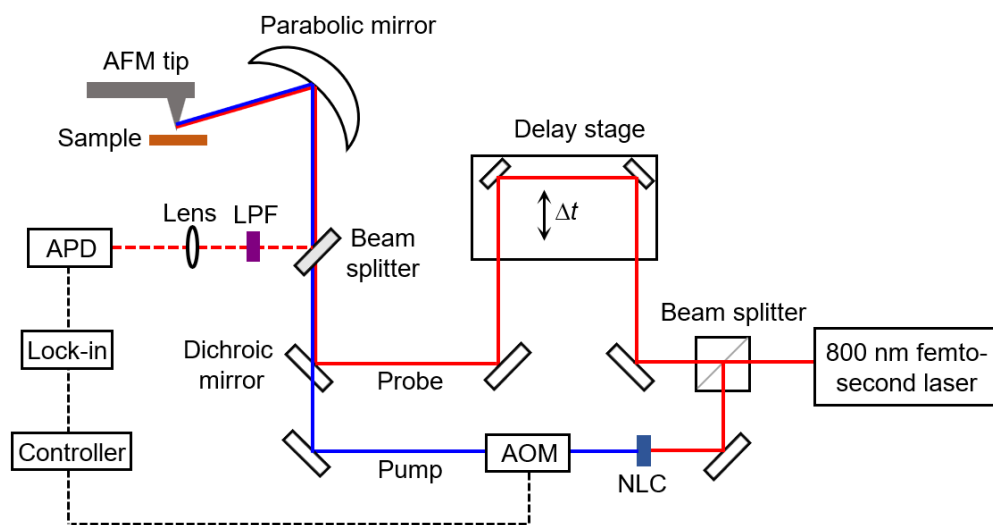
Supplementary Note 3. Exclusion of the laser heating effect

The pump excitation of photocarriers is accompanied by the laser heating effect, which causes the increase in lattice temperature. This effect of temperature rise is considered by the Jellison-Modine model (Equation S4 and S5), and the obtained dielectric function is used to calculate s-SNOM amplitude based on the point-dipole model. We model the s-SNOM amplitude change for a temperature range of 300-800 K. Only a slight increase of 1.3% is observed (Supplementary Fig. 6). In practice, the laser heating is minor, and the temperature is supposed to be much lower. Thus, we ignore the effects of temperature rise in our analysis.

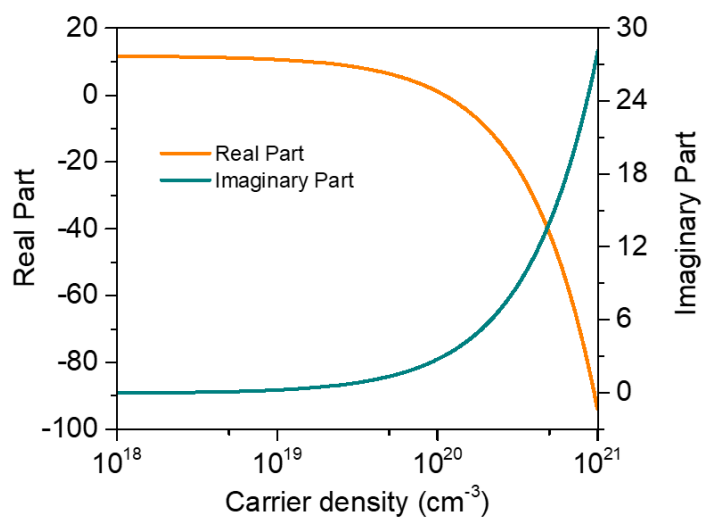
Supplementary Note 4. Exclusion of the thermal expansion effect

The temperature increase can also lead to the thermal expansion of the sample, thus reducing the tip-sample distance. This effect is directly considered in the point-dipole model by sweeping the d . Considering the thermal expansion of silicon to be $2.6 \times 10^{-6} K^{-1}$, the change in the tip-sample distance is expected to be very small and less than 0.2 nm. This change only leads to a slight change of s-SNOM amplitude of 1.6% (Supplementary Fig. 6), which indicates that thermal expansion can also be neglected.

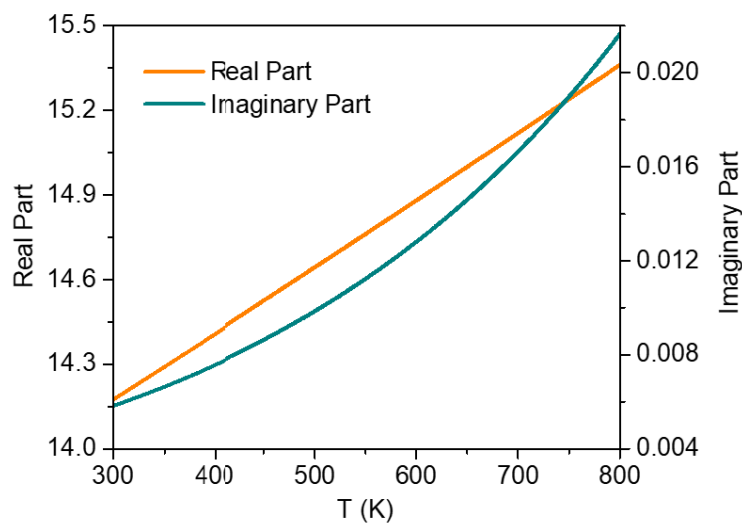
Supplementary Tables and Figures



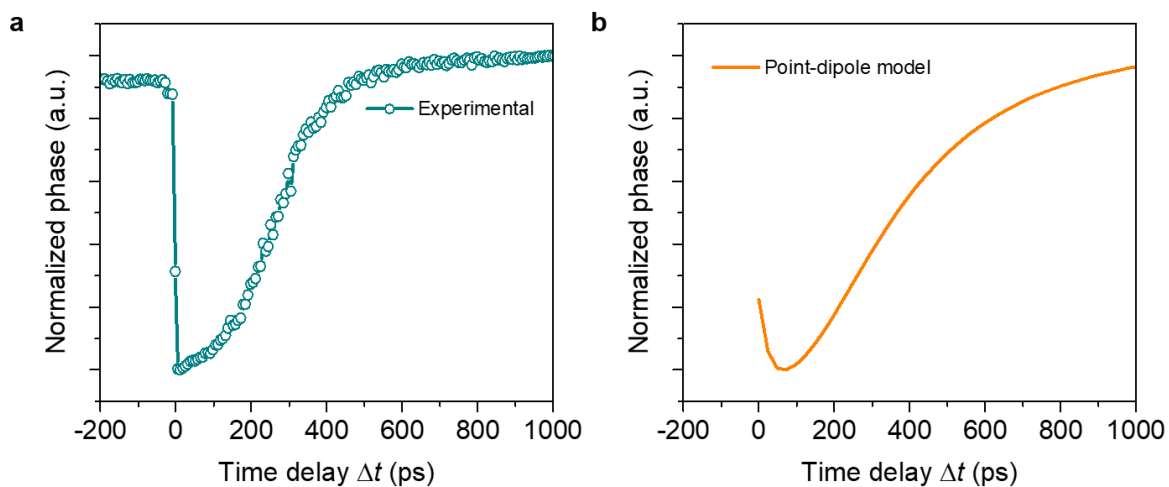
Supplementary Fig. 1. Experimental setup of pump-probe s-SNOM. NLC: non-linear crystal; AOM: acoustic-optic modulator; APD: avalanche photodiode; LPF: long-pass filter.



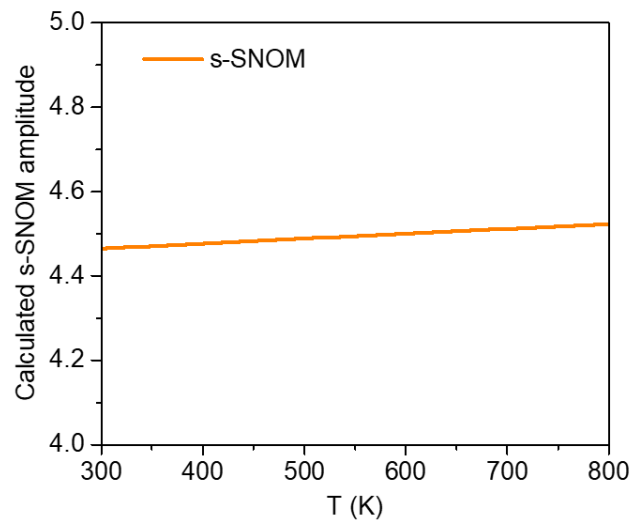
Supplementary Fig. 2. Dielectric function of silicon as a function of carrier density calculated by the Drude model.



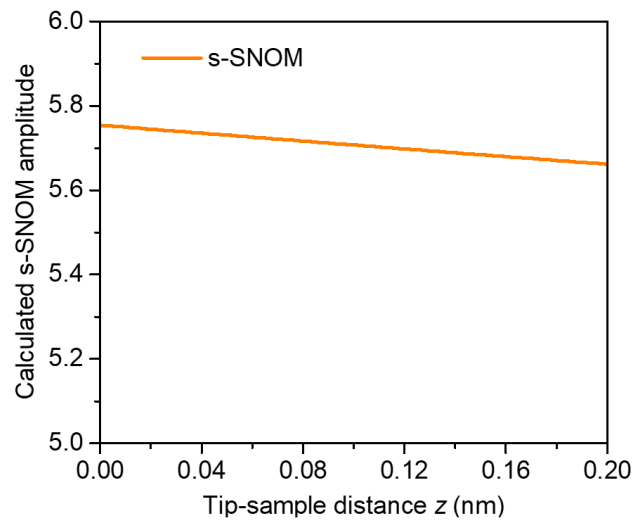
Supplementary Fig. 3. Dielectric function of silicon as a function of temperature calculated by the Jellison-Modine model.



Supplementary Fig. 4. a, Experimentally measured time-resolved phase. **b,** The phase of scattered light calculated by the point-dipole model.



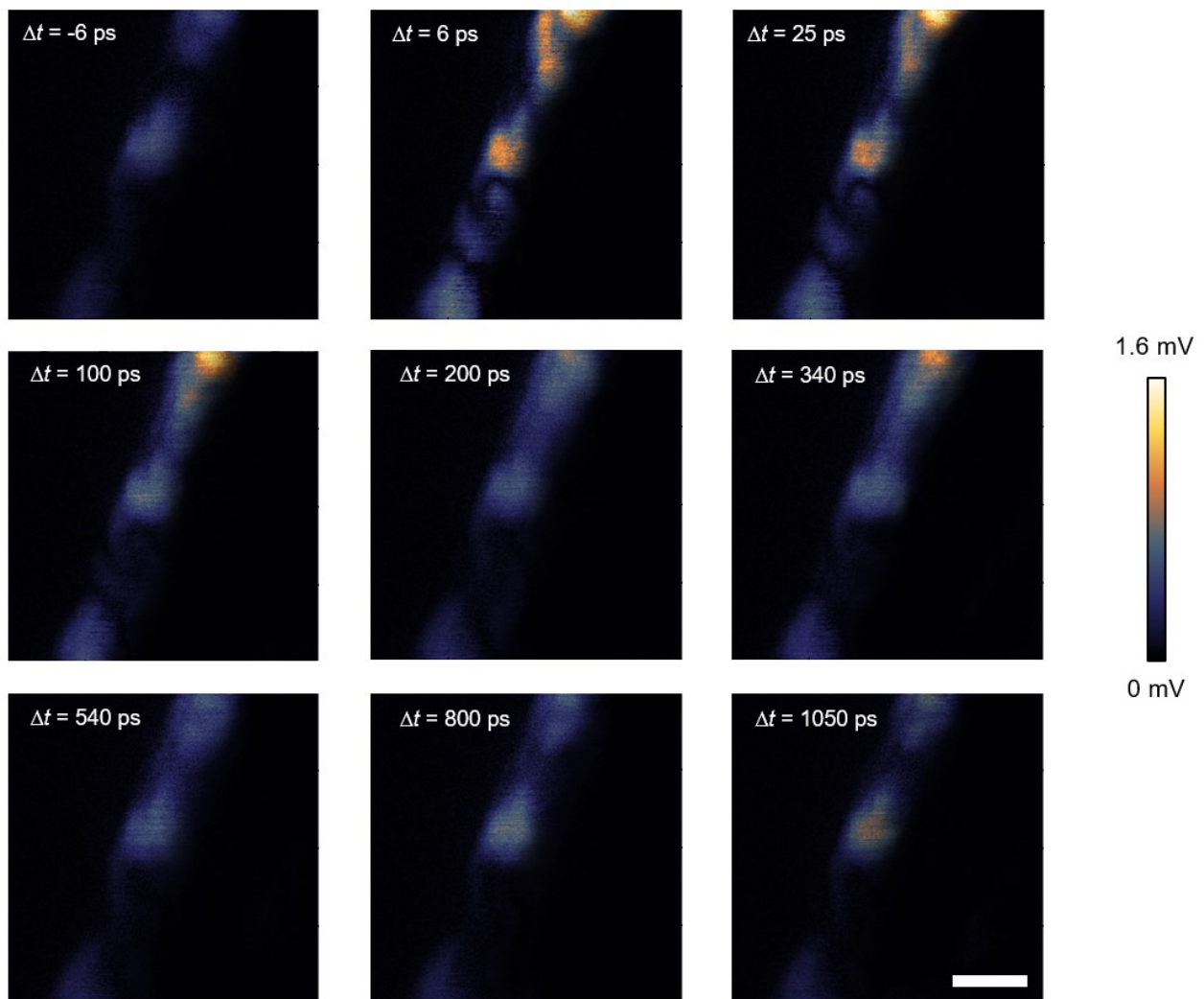
Supplementary Fig. 5. Calculated s-SNOM amplitude when the temperature increases from 300 K to 800 K.



Supplementary Fig. 6. Calculated s-SNOM amplitude when the tip sample distance increases from 0 nm to 0.2 nm.

Supplementary Table 1. Fitting parameters in Fig. 2. ($N(t) = N(0) \times (A_1 e^{-\frac{t}{t_1}} + A_2 e^{-\frac{t}{t_2}})$, and $A_1 + A_2 = 1$)

Data	$N(0) (\times 10^{19} \text{ cm}^{-3})$	A_1	t_1 (ps)	A_2	t_2 (ps)	t_{avg} (ps)
Fig. 2c	7.56	0.1	36.6	0.9	734.3	252.66
Fig. 2d (low power)	4.70	0.05	35.4	0.95	544.2	316.64
Fig. 2d (high power)	6.50	0.05	35.4	0.95	544.2	316.64



Supplementary Fig. 7. Time-resolved s-SNOM imaging of a nonuniform silicon nanostructure. Scale bar: $2\mu\text{m}$.

Supplementary References

- 1 Huber, A. J. et al. Simultaneous ir material recognition and conductivity mapping by nanoscale near-field microscopy. *Adv. Mater.* **19**, 2209-2212 (2007).
- 2 Knoll, B. & Keilmann, F. Infrared conductivity mapping for nanoelectronics. *Appl. Phys. Lett.* **77**, 3980-3982 (2000).
- 3 Cvitkovic, A., Ocelic, N. & Hillenbrand, R. Analytical model for quantitative prediction of material contrasts in scattering-type near-field optical microscopy. *Opt. Express* **15**, 8550-8565 (2007).
- 4 van Exter, M. & Grischkowsky, D. Carrier dynamics of electrons and holes in moderately doped silicon. *Phys. Rev. B* **41**, 12140-12149 (1990).
- 5 Arora, N. D., Hauser, J. R. & Roulston, D. J. Electron and hole mobilities in silicon as a function of concentration and temperature. *IEEE Trans. Electron Devices* **29**, 292-295 (1982).
- 6 Jr., G. E. J. & Modine, F. A. Optical functions of silicon at elevated temperatures. *J. Appl. Phys.* **76**, 3758-3761 (1994).